PHOTONICS Research

# Metalens-based stereoscopic microscope

Yong Long,[1] Jianchao Zhang,[1] Zhihao Liu,[1] Weibin Feng,[1] Songming Guo,[1] Qian Sun,[1] Qinfei Wu,[1] Xiangyang Yu,[1] Jianying Zhou,[1,2] Emiliano R. Martins,[3] Haowen Liang,[1,2,4] and Juntao Li[1,5]

[1]State Key Laboratory of Optoelectronic Materials and Technologies, School of Physics, Sun Yat-sen University, Guangzhou 510275, China
[2]Southern Marine Science and Engineering Guangdong Laboratory (Zhuhai), Zhuhai 519080, China
[3]São Carlos School of Engineering, Department of Electrical and Computer Engineering, University of São Paulo, São Carlos, SP 13566-590, Brazil
[4]e-mail: lianghw26@mail.sysu.edu.cn
[5]e-mail: lijt3@mail.sysu.edu.cn

Received 21 February 2022; revised 28 April 2022; accepted 29 April 2022; posted 29 April 2022 (Doc. ID 456638); published 26 May 2022

**Stereoscopic microscopy is a promising technology to obtain three-dimensional microscopic images. Such microscopes are based on the parallax effect, and as such require two lenses to focus at two different points. Geometrical constraints, however, restrict their numerical apertures to about 0.2, thus limiting the system's resolution. Higher numerical apertures (~0.35) can be achieved with designs using only one bulk lens, but such systems are ~10 times more costly than the conventional ones. Thus, there is a pressing need for alternative solutions to improve the resolution of stereoscopic systems. Here, we show that high-resolution and low-cost stereoscopic systems can be obtained using birefringent single-layer metalenses. We design and fabricate a birefringent metalens operating at 532 nm with a numerical aperture as high as 0.4. The metalens is then used to demonstrate high-resolution stereoscopic imaging of biological samples. The microscopic images are further displayed and perceived vividly in an autostereoscopic display. Our demonstration paves the way to a new strategy to achieve high-resolution and low-cost stereoscopic microscopes.** 

https://doi.org/10.1364/PRJ.456638

## 1. INTRODUCTION

Three-dimensional (3D) microscopic imaging [1–3] is a widely used technique to explore the depth information and surface topography of microscopic objects. Some representative methods are confocal scanning microscopy [4,5], light-field microscopy [6,7], structured illumination microscopy [8,9], and binocular stereoscopic microscopy [10,11]. Among these methods, stereoscopic microscopy is one of the simplest ways to record the surface and depth information of the objects in real time, with applications in the biosciences [12], medical research [13], and industrial detection [14].

Stereoscopic microscopes rely on two oblique optical axes to generate a pair of microscopic images with parallax. They can be classified into Greenough types and common main objective (CMO) types. The former uses two objectives to form light paths for left and right images, but their physical dimensions have to be restricted, to prevent contact between the lenses. Consequently, numerical apertures (NAs) are limited to ~0.2. Higher NAs (~0.35) can be achieved with the CMO type, which uses a single and large aperture objective to handle the two light paths. However, CMO microscopes are more expensive than Greenough microscopes because of the complex design and fabrication of the objectives. Thus, it is important to find alternative strategies to enable high-resolution and low-cost stereoscopic microscopes.

Metasurfaces [15–17], which use ultrathin meta-atoms to accurately modulate amplitude, phase, and polarization of the local electromagnetic fields, can achieve diverse functions such as light bending [18,19], holograms [20,21], and polarization conversion [22,23]. They are also used to enhance the quality of the stereoscopic systems, e.g., 3D stereoscopic holography [24,25]. Metalens [26–28] is a special category of metasurfaces that has been receiving much attention due to their excellent focusing and imaging abilities. Researchers have used metalenses as core elements to build various microscopic systems for biomedical and chemical imaging, such as for *ex vivo* mice intestine tissues [29], fluorescent polyethylene microspheres [30], and frog egg cells [31]. Furthermore, compared with the bulky glass lenses, metalenses are also able to implement multiple functions, such as multi-focus generation [32,33], spectral analysis [34], chiral imaging [35], and depth sensing [36]. Another major advantage of metalenses over their bulky counterparts is their ability to distinguish between polarization states, which opens up new possibilities of applications. For example, a Stokes camera based on metalenses [37], and a birefringent metalens encoding two phase profiles for corrections of aberrations were recently demonstrated [38]. Thus, the extra degree of freedom afforded by polarization control is poised to play a crucial role in the next steps of metalens research and development.

In this paper, we propose a birefringent metalens to improve the imaging performance of a Greenough-type stereoscopic microscope [Fig. 1(a)]. The designed metalens encodes two phase profiles in a single layer, thus removing the physical restrictions limiting the NA in conventional stereoscopic microscopes. Our stereoscopic metalens has an NA of 0.4 and can produce two symmetrical focal points for stereoscopic imaging at the wavelength of 532 nm. We demonstrate stereoscopic microscopic imaging by embedding the metalens in a commercial stereoscopic microscope, thus increasing its NA from 0.15 to 0.4. The system achieves a resolution of 870 nm. As a proof of concept, we use the metalens-based stereoscopic microscope to image pollen grains and silk fibers. Furthermore, a high-resolution autostereoscopic display, which can display stereoscopic microscopic images vividly without the aid of extra equipment, is assembled to enhance the viewing experience. Our approach paves the way toward high-resolution and low-cost stereoscopic microscopes.

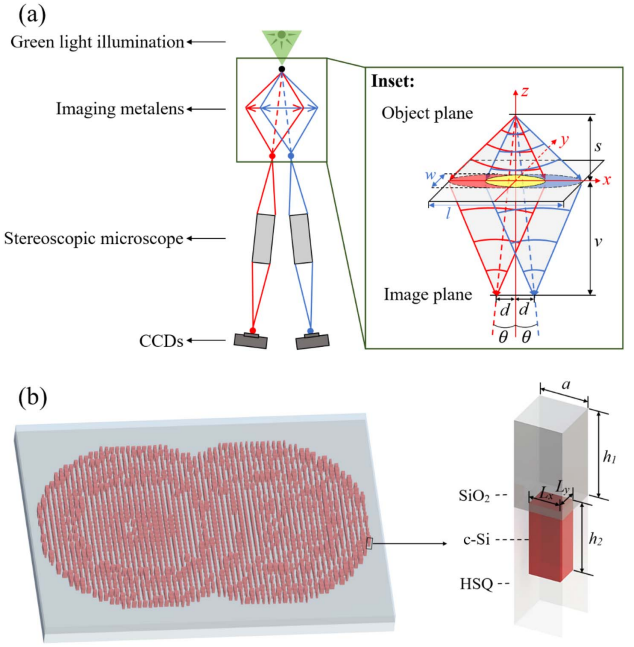


**Fig. 1.** Illustration of the imaging system, birefringent metalens, and model of a meta-atom. (a) Simplified stereoscopic microscope imaging system with birefringent metalens. The system shows a secondary imaging process, where the two symmetrical images of the target are first generated by the metalens which is illuminated by green light in the transmission mode, and then imaged again in CCDs with a commercial stereoscopic microscope. In the inset, red and blue arrows are the borderlines of the corresponding left and right metalenses, which have tilted optical axes and operate for linearly $x$- and $y$-polarized light, respectively. The yellow area illustrates the region of overlap between the two-phase profiles. The lengths of the birefringent metalens along the $x$- and $y$-axes are $w$ and $l$. Here, $w$ is also the diameter of a single left or right metalens. (b) Schematic diagram of the metalens, and model of a meta-atom for the birefringent metalens. The cured hydrogen silsesquioxane (HSQ) and $SiO_2$ films are used as the substrate and protective layers. The parameters are $h_1 = 375$ nm, $h_2 = 300$ nm, $a = 200$ nm, $L_x = 50$–$180$ nm, and $L_y = 50$–$180$ nm.

## 2. THEORETICAL DESIGN AND SIMULATION

The metalens-based stereoscopic system is illustrated in Fig. 1(a). The inset shows the metalens surface, where the colors indicate the two-phase profiles, which partially overlap in the yellow region. This overlap is significant to achieve high NA. The phase profiles are encoded in two orthogonal linear polarizations, with the left one corresponding to $x$-polarized and the right one for $y$-polarized. The metalens is designed for operation at the single wavelength of 532 nm; thus, the system does not suffer from chromatic aberrations. To make the design compatible with the commercial stereoscopic microscope setup, the center of each metalens is positioned assuming an angle of incidence of 6° [see inset Fig. 1(a)]; the diameter and NA of the metalens are 400 μm and 0.4, respectively. This birefringent metalens can image two aspects of the same object using the parallax effect.

The design of phase profiles is based on the spherical wave method [31,36,39], which is suitable for our imaging conditions based on metalenses without tube lenses and helps to eliminate spherical aberration. The phase profiles for each metalens are encoded as an aplanatic phase distribution [31] as follows:

$$\varphi_{l-m}(x,y) = \frac{2\pi}{\lambda_0}\left(\frac{s}{\cos\theta} - \sqrt{x^2+y^2+s^2}\right) + \frac{2\pi\cdot n_{\text{sub}}}{\lambda_0} \times \left[\frac{v}{\cos\theta} - \sqrt{(x+d)^2+y^2+v^2}\right], \quad (1)$$

$$\varphi_{r-m}(x,y) = \frac{2\pi}{\lambda_0}\left(\frac{s}{\cos\theta} - \sqrt{x^2+y^2+s^2}\right) + \frac{2\pi\cdot n_{\text{sub}}}{\lambda_0} \times \left[\frac{v}{\cos\theta} - \sqrt{(x-d)^2+y^2+v^2}\right], \quad (2)$$

where $d$ is the shift distance and $\theta$ is the angle of inclination; $\lambda_0$ is the wavelength in air; and $s$ and $v$ are, respectively, the object and image distances [see inset of Fig. 1(a)]. In our design, these parameters are set to be $s/v = 3$; $n_{\text{sub}}$ is the refractive index of the substrate. To simplify the design, we treat the thickness of the substrate as infinite and uniform; hence, the image plane is inside the substrate. It is noted that, unlike the hyperbolic metalens, the NAs of these aplanatic metalenses are defined by the object distance $s$ and the diameter $w$ of each metalens as $\text{NA} = w/\sqrt{w^2+4s^2}$ [31].

The geometry of the birefringent meta-atoms is shown in Fig. 1(b). To protect the metalens from accidental collision and friction, a silica layer is deposited to cover the nanopillars. Crystalline silicon (c-Si) is chosen as the material of the nanopillar because of its high refractive index and strong field confinement, which can effectively achieve precise phase control and high transmission efficiency of the metasurfaces with a protective layer at the visible wavelength [40]. To simultaneously achieve high transmission and accurate phase control of the nanopillars, the period of the meta-atom and the height of the nanopillar are set to be $a = 200$ nm and $h_2 = 300$ nm, respectively. As shown in Fig. 2, by varying $L_x$ and $L_y$, the effective index of the c-Si cuboid nanopillar can be changed, yielding a full $2\pi$ coverage phase with high transmission at the wavelength of 532 nm. The rotational symmetry of the cubic

nanopillars allows the same library of meta-atoms to be used for both polarizations [41]. The chosen structures for four phase levels spanning the full $2\pi$ phase coverage are marked with the colored symbols (listed in Table 1) in Fig. 2.

The focusing performance of the designed birefringent metalens is evaluated using 3D finite-difference time-domain (FDTD). The refractive index of c-Si used in the simulation is 4.15. To save computation time, we consider a birefringent metalens with an NA of 0.4 and sizes of $l \times w = 12.8\ \mu\text{m} \times 10\ \mu\text{m}$ [inset of Fig. 1(a)], which correspond to the diameter of the single left or right metalens, to be $w = 10\ \mu\text{m}$. The phase profiles of the proposed metalens are shown in Fig. 3(a). Notice that only the yellow region, where both phase profiles overlap, requires simultaneous lensing effect for both polarizations, whereas the red (blue) region requires lensing effect only for $x$-polarized ($y$-polarized) light. The deviation between the designed and ideal phase profiles introduces imaging aberrations. To optimize the matching between the design and ideal phase profiles, the metalens in the red region is designed so that its phase for $x$-polarized light satisfies Eq. (1), but no constraints are imposed on the $y$ polarization. Likewise, the metalens in the blue region is designed to satisfy Eq. (2) for $y$-polarized incidence. Dipole sources with linear $x$ and $y$ polarizations are placed on the left and right of the designed image points and utilized in the simulation for focusing characterization.

As shown in Figs. 3(b) and 3(d), the metalens successfully discriminates between the polarization of the incident beam, correctly focusing it in the target position. By fitting with Airy functions, the full width at half-maximum of the two focal spots is calculated to be 655.2 nm and 608.4 nm, respectively [Figs. 3(c) and 3(e)]. The simulated focusing efficiencies of the left and right metalenses are 33.2% and 32.2%, respectively.

**Table 1. Symbol Definition Relative to Fig. 2[a]**

| Phase Levels | $X$ Polarization | $Y$ Polarization |
|---|---|---|
| 0 or $2\pi$ | Red | Diamonds |
| $\pi/2$ | Green | Circles |
| $\pi$ | Blue | Up triangles |
| $3\pi/2$ | Black | Left triangles |

[a]Each color (symbol) corresponds to a phase for $x$- and $y$-polarized light.

## 3. FABRICATION PROCESS

To fabricate the metalens, a bonding process [19,42] is carried out on a silicon-on-insulator wafer with a 400 nm c-Si thin-film and a 375 nm thick silicon dioxide layer. First, inductively coupled plasma (ICP, Oxford Instruments Plasma Pro System 100 ICP180) is used to etch down the c-Si layer to 300 nm. The pattern is defined in a high-resolution negative resist (HSQ) with 230 nm thickness using electron beam lithography (Raith Vistec EBPG-5000plusES). After exposure, the pattern is transferred to a c-Si layer by ICP etching. The HSQ is spun onto the structures, followed by hard baking at 300°C for 5 h to flatten the surface. Whereas $SiO_2$ and other common materials are developed by chemical vapor deposition, the HSQ layer is processed by spin coating and hard baking, which can easily infiltrate into the gaps between the meta-atoms and has better back-filling performance [43]. Then a silica buffer layer is deposited on the sample by inductively coupled plasma chemical vapor deposition (ICP-CVD, Oxford Instruments Plasma Pro System 100 ICP180-CVD). The UV light curable adhesive NOA61 is spin-coated on the sample to bond with the glass

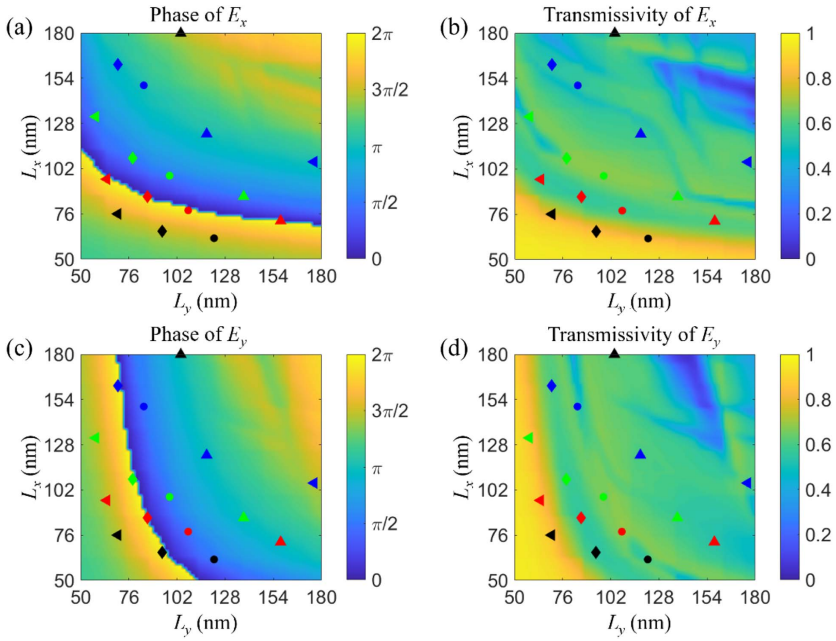


**Fig. 2.** Calculation of (a), (c) the phase and (b), (d) the transmission of the c-Si cuboid nanopillars with different sizes by the linearly $x$- and $y$-polarized plane wave incidence, respectively. The period and height of the meta-atom are set to be 200 nm and 300 nm. The colored symbols represent the chosen structures for achieving four phase levels spanning the full $2\pi$ phase coverage. Their correspondences are listed in Table 1.

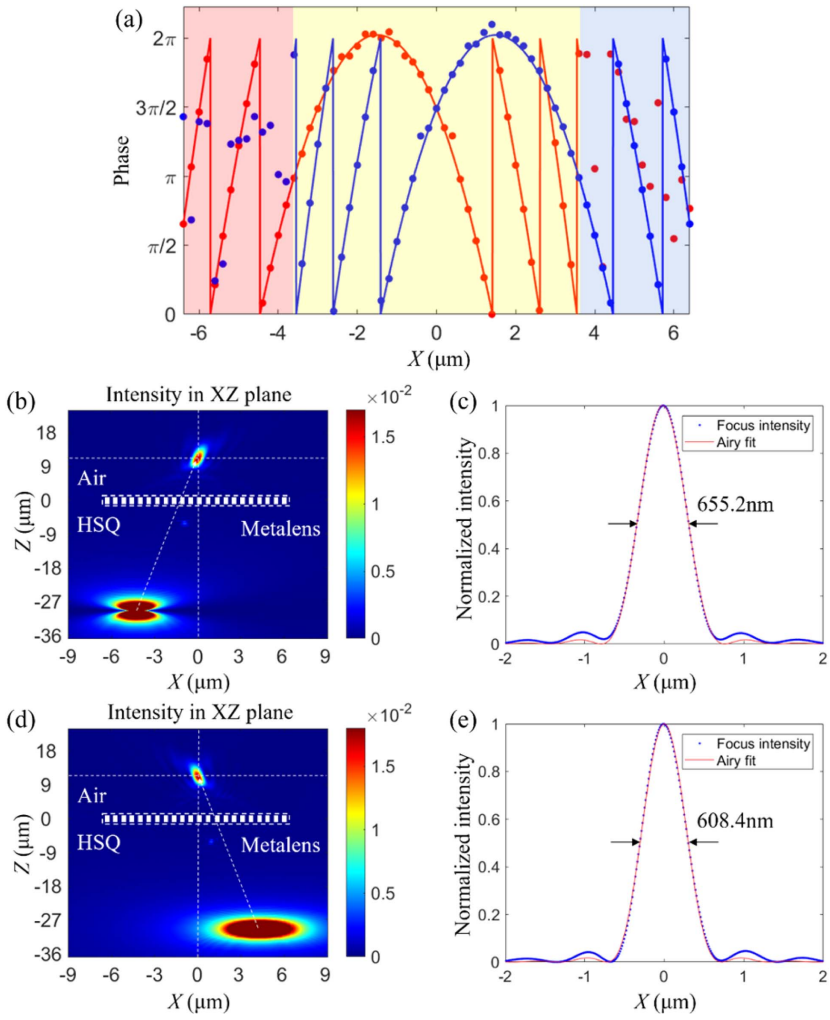


**Fig. 3.** (a) Ideal phase profile (lines) of the proposed birefringent metalens and the actual phase responses (dots) of the chosen meta-atoms. Red and blue correspond to the phases for the *x*- and *y*-polarized light according to Eq. (1) and Eq. (2), respectively. The yellow region illustrates the overlapping area of the phase profiles of the birefringent metalenses. (b)–(e) FDTD simulation of the focusing ability of the metalens. (b) Electric field intensity distribution of the linearly *x*-polarized dipole source (the spot on the bottom) passing through the metalens and focusing in the target position (the spot on the top). (c) The normalized intensity distributions of (b) along the *x*-axis at the focal plane. (d), (e) The corresponding simulation results for a *y*-polarized dipole source.

substrate by subsequent ultraviolet LED light illumination. Finally, the opaque silicon substrate is removed by the precise grinding machine Logitech PM6 and ICP. Scanning electron microscope (SEM) images of the metalens with a diameter of 400 μm are shown in Fig. 4.

## 4. STEREOSCOPIC MICROSCOPE IMAGING

The designed birefringent metalens is embedded in a commercial stereoscopic microscope according to the optical setup of Fig. 1(a) to perform high-resolution stereoscopic microscope imaging operating in the transmission mode. The stereoscopic microscope (Yong Heng XTZ-05T) is of Greenough-type with an NA of 0.15. It has two individual light paths and two objectives. A white-light LED source associated with a 532 nm filter with 10 nm bandwidth is used for incoherent and unpolarized green light illumination. The sample is placed near the object distance, which is $s = 450$ μm, in accordance with the diameter $w$ of 400 μm and NA of 0.4. The images from the birefringent metalenses are matched with the parallax angles of the stereoscopic microscope so that the left and right images with *x*- and *y*-polarized light can be collected by the microscope objectives of the stereoscopic microscope.

A 1951 USAF resolution chart is used to measure the resolution and magnification of the proposed setup. Figure 5(a) shows the images obtained with the stereoscopic microscope without the metalens. The resolution is limited and only the fringes in Group 7 Element 6 (228.1 lp/mm, corresponding to a resolution of 2192 nm) can be distinguished. After embedding the metalens, the fringes in Group 9 Element 2 (574.7 lp/mm, corresponding to the resolution of 870 nm) can be imaged clearly, as shown in Figs. 5(b) and 5(c). Thus, the resolution of the system is higher than 870 nm, which is close to the Rayleigh criterion for an NA of 0.4 at the wavelength of 532 nm ($0.61\lambda$/NA). Besides the optical resolution

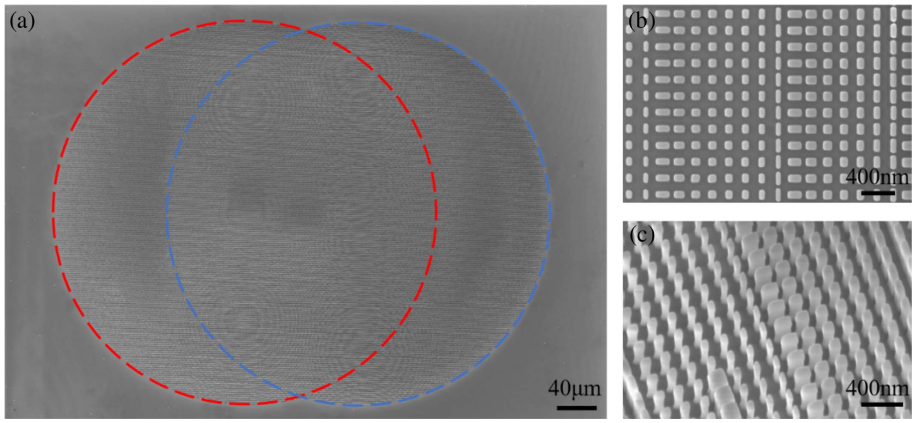


**Fig. 4.** SEM images of the fabricated birefringent metalens. (a) Overall outlines of the metalenses. Red and blue dashed circles outline the effective regions of the left and right metalenses. Each of them has a diameter of 400 μm. (b) Top view and (c) 30° titled view of the metalens at a higher magnification. The HSQ resist is not removed.

and magnification, the stereoscopic depth $z = bf/Md$ and the depth resolution $\Delta z = z(Md) - z(Md + M\Delta d)$ are other important metrics for characterizing the performance of stereoscopic microscopes [44]. In the experiment, $b = 95.1$ μm is the separation baseline of the centers of the two metalenses, $f = 310.5$ μm is the focal length, $M = 13.6$ is the magnification, $d = 43.2$ μm is the disparity, and $\Delta d = 3.6$ μm is the disparity step which equals the pixel size. Accordingly, the stereoscopic depth $z$ is 50.3 μm and the depth resolution $\Delta z$ is about 3.9 μm.

To demonstrate the application of the metalens assisted stereoscopic microscope, micro-samples of pollen grains and silk fibers are chosen as targets. The dimensions of pollens are around 18 μm to 30 μm, while the width of a silk fiber is around 10 μm to 20 μm. Their featured sizes are compatible with the resolution of the setup, and they are stacked or staggered with suitable depth information.

To better understand our stereoscopic microscope compared with conventional optical microscopes, we used both systems to image pollen grains and silk fibers. As shown in Fig. 6, the birefringent metalens can enhance the resolution and magnification of the stereoscopic microscope to the level of a conventional optical microscope.

The left and right parallax images of the pollen grains [Figs. 6(b) and 6(c)] and silk fibers [Figs. 6(f) and 6(g)] are further sent to the autostereoscopic display (Fig. 7), which follows the principle of temporal–spatial multiplexing directional backlight design [45]. Assisted by this autostereoscopic display, vivid and full high-definition stereoscopic microscopic images can be perceived without wearing extra equipment, thus greatly simplifying the system and improving the perceptual experience [46,47].

Since the stereo perception can only be reached with a specialized display, we transform the full-color stereoscopic microscopic images into anaglyph images [Figs. 6(i) and 6(j)], so that stereo perception can be obtained with the assistance of red–blue glasses via normal screens. Other stereoscopic displays, such as polarized-glasses assisted displays [48] and virtual reality equipment [49,50], are also compatible with our proposed stereoscopic microscope.

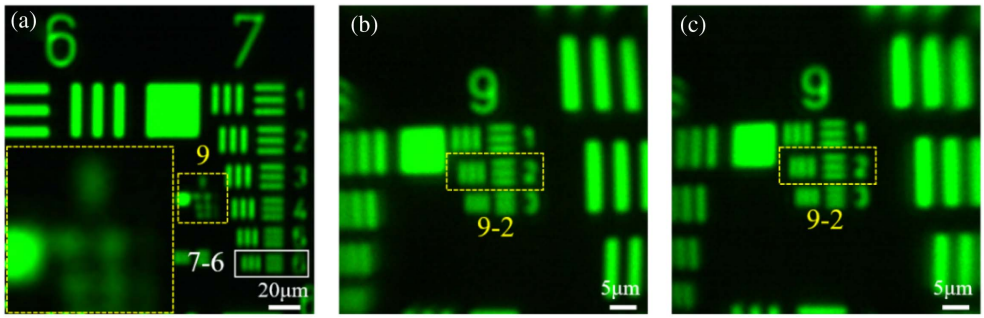


**Fig. 5.** Resolution characterization using images of the 1951 USAF resolution chart. (a) Fringes imaged by stereoscopic microscope without the birefringent metalens, operating at 6.2× magnification. The fringes in Group 7 Element 6 enclosed by the white solid frame are just clear while the fringes in Group 9 enclosed by the yellow dotted frame are all blurry. The inset shows a zoom-in image of Group 9. (b) Fringes imaged by the stereoscopic microscope with the birefringent metalens and from the left light path of the system for the *x*-polarized light. In this situation, the fringes enclosed by the yellow dotted frame in Group 9 Element 2 can be distinguished. (c) The corresponding fringes image of (b) from the right light path of the system for the *y*-polarized light. The magnifications of (b) and (c) are both 13.6×, where the extra 2.2× magnification is enabled by the metalens.

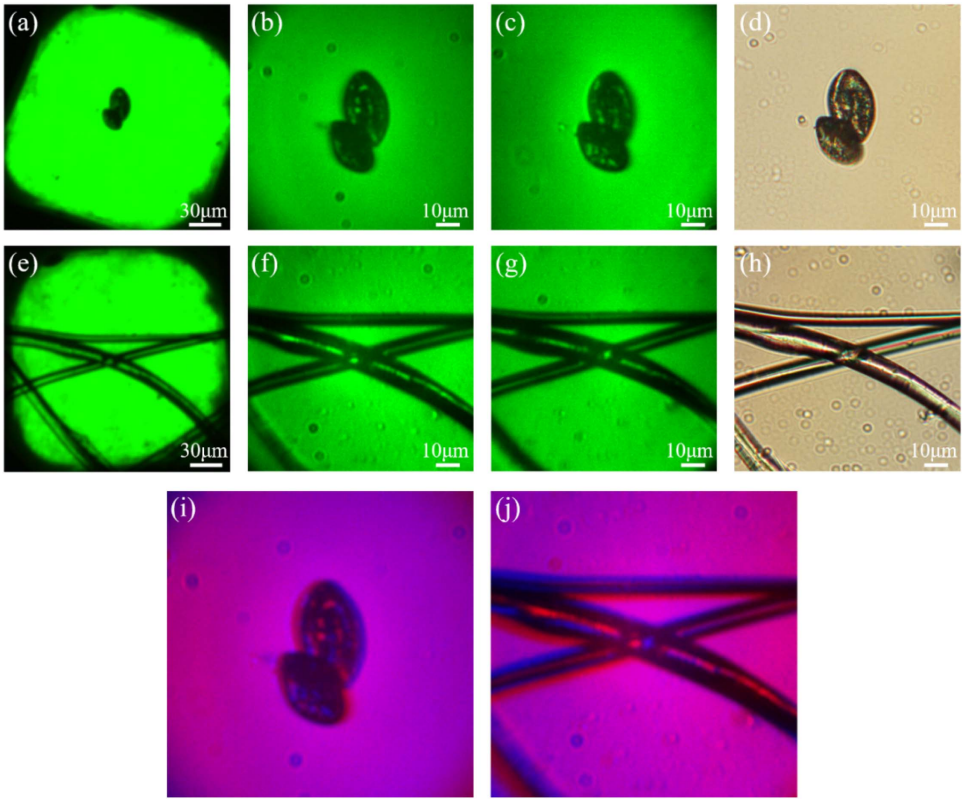


**Fig. 6.** Imaging results of pollen grains and silk fibers. Images of pollen grains taken from (a) the right light path of stereoscopic microscope without metalens of NA of 0.15 and magnification of 6.2×, (b) left and (c) right light paths of stereoscopic microscope with metalens of NA of 0.4 and magnification of 13.6×, (d) conventional binocular microscope with NA of 0.45 and magnification of 20× in transmission mode. (e)–(h) Images of silk fibers taken by the same methods as in (a)–(d). Red–blue composite pictures of (i) pollen grains and (j) silk fibers from (b), (c) and (f), (g). A stereoscopic perception can be obtained by wearing red–blue glasses (see Visualization 1 and Visualization 2 for more results).

## 5. DISCUSSION

In terms of the image quality, it is worth noting that our stereoscopic microscopic images are obtained under the transmission mode. Since the pollen grains and silk fibers are not completely transparent, the contrast of the images is decreased and some superficial details are missing, resulting in inevitable deterioration of image quality. The reflection mode metalens [51,52] or the hybrid of the metalens [53–56] and the conventional refractive lens [57] will assist in increasing the ability to operate in reflection, which can improve the image quality further. Furthermore, in the phase design, we assume that a spherical wave is emitted by a single point. An improved design could

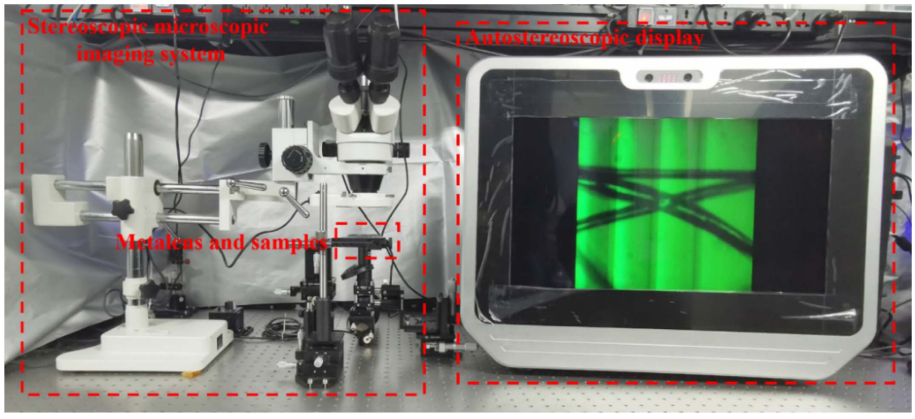


**Fig. 7.** Stereoscopic microscope (Yong Heng XTZ-05T) is of Greenough-type with NA of 0.15. It has two individual light paths and two objectives. The metalens is placed in front of the objective to enhance the NA and magnification of the stereoscopic microscope. The captured left and right parallax images from the metalens-based stereoscopic microscope are sent to the autostereoscopic display to perceive vivid and full high-definition stereoscopic microscopic images without wearing extra equipment.

be obtained by taking into account emission from multiple points, so as to eliminate comatic aberrations.

In addition, the NA and magnification are closely related to the depth of field of the microscopic image. Our metalens has an NA of 0.4, which can resolve the sizes and depth positions of the pollen grains and silk fibers samples. Higher resolution can be achieved by reducing the distance between the birefringent metalens and the object plane. In principle, the resolution can be further improved by compounding birefringent metalens with higher NA metalenses for imaging [31,58–61], and theoretically the NA can reach 1.33 according to the Nyquist sampling $\mathrm{NA} \le \lambda/(2 \cdot a)$ [58]. However, the corresponding stereoscopic depth will decrease accordingly, which is significant for smaller targets with smaller depth positions. For example, for the hemoglobin with the size of 7 μm, a metalens with NA of 0.6 is more suitable.

## 6. CONCLUSION

In conclusion, we propose a birefringent metalens to improve the imaging resolution in the stereoscopic microscope. The designed single-layer metalens encodes two lensing phase profiles together, thereby removing the physical limitations of the bulk lens and thus achieving a higher NA than objectives used in the conventional stereoscopic microscopes. The demonstration shows that the birefringent metalens is compatible with commercial stereoscopic systems and can improve its resolutions while maintaining low cost.

**Funding.** National Key Research and Development Program of China (2020YFC2007102); National Natural Science Foundation of China (11704421, 11974436, 12074444); Basic and Applied Basic Research Foundation of Guangdong Province (2020A1515011184, 2020B1515020019); Innovation Group Project of Southern Marine Science and Engineering (Guangdong); Sao Paulo Research Foundation FAPESP (2020/00619-4, 2021/06121-0); CNPq (307602/2021-4).

**Acknowledgment.** H. L. acknowledges support by Innovation Group Project of Southern Marine Science and Engineering (Guangdong). E. R. M. acknowledges support by FAPESP and CNPq.

**Disclosures.** The authors declare no conflicts of interest.

**Data Availability.** Data underlying the results presented in this paper are not publicly available at this time but may be obtained from the authors upon reasonable request.

## REFERENCES

1. N. Pears, Y. Liu, and P. Bunting, *3D Imaging, Analysis and Applications* (Springer, 2012).
2. Y. Hiraoka, J. W. Sedat, and D. A. Agard, "Determination of three-dimensional imaging properties of a light microscope system," Biophys. J. **57**, 325–333 (1990).
3. S. S. S. Poon, S. J. Lockett, and R. K. Ward, "Characterization of a 3D microscope imaging system," Proc. SPIE **1905**, 121–128 (1993).
4. B. S. Chun, K. Kim, and D. Gweon, "Three-dimensional surface profile measurement using a beam scanning chromatic confocal microscope," Rev. Sci. Instrum. **80**, 073706 (2009).
5. G. M. R. D. Luca, R. M. P. Breedijk, R. A. J. Brandt, C. H. C. Zeelenberg, B. E. de Jong, W. Timmermans, L. N. Azar, R. A. Hoebe, S. Stallinga, and E. M. M. Manders, "Re-scan confocal microscopy: scanning twice for better resolution," Biomed. Opt. Express **4**, 2644–2656 (2013).
6. M. Broxton, L. Grosenick, S. Yang, N. Cohen, A. Andalman, K. Deisseroth, and M. Levoy, "Wave optics theory and 3-D deconvolution for the light field microscope," Opt. Express **21**, 25418–25439 (2013).
7. G. Wu, B. Masia, A. Jarabo, Y. Zhang, L. Wang, Q. Dai, T. Chai, and Y. Liu, "Light field image processing: an overview," IEEE J. Sel. Top. Signal Process. **11**, 926–954 (2017).
8. M. F. Langhorst, J. Schaffer, and B. Goetze, "Structure brings clarity: structured illumination microscopy in cell biology," Biotechnol. J. **4**, 858–865 (2019).
9. J. Geng, "Structured-light 3D surface imaging: a tutorial," Adv. Opt. Photonics **3**, 128–160 (2011).
10. H. W. Schreier, D. Garcia, and M. A. Sutton, "Advances in light microscope stereo vision," Exp. Mech. **44**, 278–288 (2004).
11. K. W. Nam, J. Park, I. Y. Kim, and K. G. Kim, "Application of stereo-imaging technology to medical field," Healthc. Inform. Res. **18**, 158–163 (2012).
12. M. Jacob, N. Mohan, S. M. Fenn, P. Rajathi, P. Suryagopan, and L. Vishalini, "Application of stereomicroscope in the pre-analytic macroscopic examination of biopsy specimens," J. Clin. Diagn. Res. **13**, ZC01– ZC07 (2019).
13. T. Rusin and M. Kopernik, "Characterization of biocompatible materials using stereo microscope 3D digital image correlation," Adv. Eng. Mater. **18**, 1651–1660 (2016).
14. R. Windecker, M. Fleischer, and H. J. Tiziani, "Three-dimensional topometry with stereomicroscopes," Opt. Eng. **36**, 3372–3377 (1997).
15. N. Yu, P. Genevet, M. A. Kats, F. Aieta, J.-P. Tetienne, F. Capasso, and Z. Gaburro, "Light propagation with phase discontinuities: generalized laws of reflection and refraction," Science **334**, 333–337 (2011).
16. A. V. Kildishev, A. Boltasseva, and V. M. Shalaev, "Planar photonics with metasurfaces," Science **339**, 1232009 (2013).
17. H.-H. Hsiao, C. H. Chu, and D. P. Tsai, "Fundamentals and applications of metasurfaces," Small Methods **1**, 1600064 (2017).
18. X. Ni, N. K. Emani, A. V. Kildishev, A. Boltasseva, and V. M. Shalaev, "Broadband light bending with plasmonic nanoantennas," Science **335**, 427 (2012).
19. Z. Zhou, J. Li, R. Su, B. Yao, H. Fang, K. Li, L. Zhou, J. Liu, D. Stellinga, C. P. Reardon, T. F. Krauss, and X. Wang, "Efficient silicon metasurfaces for visible light," ACS Photonics **4**, 544–551 (2017).
20. R. C. Devlin, M. Khorasaninejad, W. T. Chen, J. Oh, and F. Capasso, "Broadband high-efficiency dielectric metasurfaces for the visible spectrum," Proc. Natl. Acad. Sci. USA **113**, 10473–10478 (2016).
21. Y. Zhou, I. I. Kravchenko, H. Wang, H. Zheng, G. Gu, and J. Valentine, "Multifunctional metaoptics based on bilayer metasurfaces," Light Sci. Appl. **8**, 80 (2019).
22. A. Arbabi, Y. Horie, M. Bagheri, and A. Faraon, "Dielectric metasurfaces for complete control of phase and polarization with subwavelength spatial resolution and high transmission," Nat. Nanotechnol. **10**, 937–943 (2015).
23. A. H. Dorrah, N. A. Rubin, A. Zaidi, M. Tamagnone, and F. Capasso, "Metasurface optics for on-demand polarization transformations along the optical path," Nat. Photonics **15**, 287–296 (2021).
24. A. Martins, J. Li, A. F. da Mota, V. M. Pepino, Y. Wang, L. G. Neto, F. L. Teixeira, E. R. Martins, and B.-H. V. Borges, "Broadband c-Si metasurfaces with polarization control at visible wavelengths: applications to 3D stereoscopic holography," Opt. Express **26**, 30740–30752 (2018).
25. J. Deng, Z. Li, G. Zheng, J. Tao, Q. Dai, L. Deng, P. He, Q. Deng, and Q. Mao, "Depth perception based 3D holograms enabled with polarization-independent metasurfaces," Opt. Express **26**, 11843–11849 (2018).
26. H. Liang, A. Martins, B.-H. V. Borges, J. Zhou, E. R. Martins, J. Li, and T. F. Krauss, "High performance metalenses: numerical aperture, aberrations, chromaticity, and trade-offs," Optica **6**, 1461–1470 (2019).
27. M. L. Tseng, H.-H. Hsiao, C. H. Chu, M. K. Chen, G. Sun, A.-Q. Liu, and D. P. Tsai, "Metalenses: advances and applications," Adv. Opt. Mater. **6**, 1800554 (2018).

28. P. Lalanne and P. Chavel, "Metalenses at visible wavelengths: past, present, perspectives," Laser Photonics Rev. **11**, 1600295 (2017).
29. Y. Luo, C. H. Chu, S. Vyas, H. Y. Kuo, Y. H. Chia, M. K. Chen, X. Shi, T. Tanaka, H. Misawa, Y.-Y. Huang, and D. P. Tsai, "Varifocal metalens for optical sectioning fluorescence microscopy," Nano Lett. **21**, 5133–5142 (2021).
30. E. Arbabi, J. Li, R. J. Hutchins, S. M. Kamali, A. Arbabi, Y. Horie, P. V. Dorpe, V. Gradinaru, D. A. Wagenaar, and A. Faraon, "Two-photon microscopy with a double-wavelength metasurface objective lens," Nano Lett. **18**, 4943–4948 (2018).
31. C. Chen, W. Song, J.-W. Chen, J.-H. Wang, Y. H. Chen, B. Xu, M.-K. Chen, H. Li, B. Fang, J. Chen, H. Y. Kuo, S. Wang, D. P. Tsai, S. Zhu, and T. Li, "Spectral tomographic imaging with aplanatic metalens," Light Sci. Appl. **8**, 99 (2019).
32. S. Tian, H. Guo, J. Hu, and S. Zhuang, "Dielectric longitudinal bifocal metalens with adjustable intensity and high focusing efficiency," Opt. Express **27**, 680–688 (2019).
33. C. Chen, Y. Wang, M. Jiang, J. Wang, J. Guan, B. Zhang, L. Wang, J. Lin, and P. Jin, "Parallel polarization illumination with a multifocal axicon metalens for improved polarization imaging," Nano Lett. **20**, 5428–5434 (2020).
34. M. Khorasaninejad, W. T. Chen, J. Oh, and F. Capasso, "Super-dispersive off-axis meta-lenses for compact high resolution spectroscopy," Nano Lett. **16**, 3732–3737 (2016).
35. M. Khorasaninejad, W. T. Chen, A. Y. Zhu, J. Oh, R. C. Devlin, D. Rousso, and F. Capasso, "Multispectral chiral imaging with a metalens," Nano Lett. **16**, 4595–4600 (2016).
36. Q. Guo, Z. Shi, Y.-W. Huang, E. Alexander, C.-W. Qiu, F. Capasso, and T. Zicklera, "Compact single-shot metalens depth sensors inspired by eyes of jumping spiders," Proc. Natl. Acad. Sci. USA **116**, 22959–22965 (2019).
37. N. A. Rubin, G. D'aversa, P. Chevalier, Z. Shi, W. T. Chen, and F. Capasso, "Matrix Fourier optics enables a compact full-Stokes polarization camera," Science **365**, eaax1839 (2019).
38. A. Martins, K. Li, G. S. Arruda, D. Conteduca, H. Liang, J. Li, B.-H. V. Borges, T. F. Krauss, and E. R. Martins, "Correction of aberrations via polarization in single layer metalenses," Adv. Opt. Mater. **10**, 2102555 (2022).
39. F. Aieta, P. Genevet, M. Kats, and F. Capasso, "Aberrations of flat lenses and aplanatic metasurfaces," Opt. Express **21**, 31530–31539 (2013).
40. Q. Sun, H. Liang, J. Zhang, W. Feng, E. R. Martins, T. F. Krauss, and J. Li, "Highly efficient air-mode silicon metasurfaces for visible light operation embedded in a protective silica layer," Adv. Opt. Mater. **9**, 2002209 (2021).
41. J. P. B. Mueller, N. A. Rubin, R. C. Devlin, B. Groever, and F. Capasso, "Metasurface polarization optics: independent phase control of arbitrary orthogonal states of polarization," Phys. Rev. Lett. **118**, 113901 (2017).
42. N. Li, Y. H. Fu, Y. Dong, T. Hu, Z. Xu, Q. Zhong, D. Li, K. H. Lai, S. Zhu, Q. Lin, Y. Gu, and N. Singh, "Large-area pixelated metasurface beam deflector on a 12-inch glass wafer for random point generation," Nanophotonics **8**, 1855–1861 (2019).
43. T. P. White, L. O'Faolain, J. Li, L. C. Andreani, and T. F. Krauss, "Silica-embedded silicon photonic crystal waveguides," Opt. Express **16**, 17076–17081 (2008).
44. T.-M. Wang and Z.-C. Shih, "Measurement and analysis of depth resolution using active stereo cameras," IEEE Sens. J. **21**, 9218–9230 (2021).
45. A. Zhang, J. Wang, Y. Zhou, H. Liang, H. Fan, K. Li, P. Krebs, and J. Zhou, "Illumination optics in emerging naked-eye 3D display," Prog. Electromagn. Res. **159**, 93–124 (2017).
46. H. Fan, Y. Zhou, J. Wang, H. Liang, P. Krebs, J. Su, D. Lin, K. Li, and J. Zhou, "Full resolution, low crosstalk, and wide viewing angle autostereoscopic display with a hybrid spatial-temporal control using freeform surface backlight unit," J. Disp. Technol. **11**, 620–624 (2015).
47. J. Wang, H. Liang, H. Fan, Y. Zhou, P. Krebs, J. Su, Y. Deng, and J. Zhou, "High-quality autostereoscopic display with spatial and sequential hybrid control," Appl. Opt. **52**, 8549–8553 (2013).
48. F. Wu, G.-J. Lv, H. Deng, B.-C. Zhao, and Q.-H. Wang, "Dual-view integral imaging three-dimensional display using polarized glasses," Appl. Opt. **57**, 1447–1449 (2018).
49. J. S. Henn, G. M. Lemole, M. A. T. Ferreira, L. F. Gonzalez, M. Schornak, M. C. Preul, and R. F. Spetzler, "Interactive stereoscopic virtual reality: a new tool for neurosurgical education," J. Neurosurg. **96**, 144–149 (2002).
50. A. Maimone, A. Georgiou, and J. S. Kollin, "Holographic near-eye displays for virtual and augmented reality," ACM Trans. Graph. **36**, 85 (2017).
51. K. Dou, X. Xie, M. Pu, X. Li, X. Ma, C. Wang, and X. Luo, "Off-axis multi-wavelength dispersion controlling metalens for multi-color imaging," Opto-Electron. Adv. **3**, 19000501 (2020).
52. M. Khorasaninejad, Z. Shi, A. Y. Zhu, W. T. Chen, V. Sanjeev, A. Zaidi, and F. Capasso, "Achromatic metalens over 60 nm bandwidth in the visible and metalens with reverse chromatic dispersion," Nano Lett. **17**, 1819–1824 (2017).
53. S. Boroviks, R. A. Deshpande, N. A. Mortensen, and S. I. Bozhevolnyi, "Multifunctional metamirror: polarization splitting and focusing," ACS Photonics **5**, 1648–1653 (2018).
54. J. Hu, X. Ren, A. N. Reed, T. Reese, D. Rhee, B. Howe, L. J. Lauhon, A. M. Urbas, and T. W. Odom, "Evolutionary design and prototyping of single crystalline titanium nitride lattice optics," ACS Photonics **4**, 606–612 (2017).
55. J. Hu, D. Wang, D. Bhowmik, T. Liu, S. Deng, M. P. Knudson, X. Ao, and T. W. Odom, "Lattice-resonance metalenses for fully reconfigurable imaging," ACS Nano **13**, 4613–4620 (2019).
56. M. D. Huntington, L. J. Lauhon, and T. W. Odom, "Subwavelength lattice optics by evolutionary design," Nano Lett. **14**, 7195–7200 (2014).
57. N. Sergienko, V. Dhayalan, and J. J. Stamnes, "Comparison of focusing properties of conventional and diffractive lenses," Opt. Commun. **194**, 225–234 (2001).
58. W. T. Chen, A. Y. Zhu, M. Khorasaninejad, Z. Shi, V. Sanjeev, and F. Capasso, "Immersion meta-lenses at visible wavelengths for nanoscale imaging," Nano Lett. **17**, 3188–3194 (2017).
59. M. Khorasaninejad, W. T. Chen, R. C. Devlin, J. Oh, A. Y. Zhu, and F. Capasso, "Metalenses at visible wavelengths: diffraction-limited focusing and subwavelength resolution imaging," Science **352**, 1190–1194 (2016).
60. M. Khorasaninejad, A. Y. Zhu, C. Roques-Carmes, W. T. Chen, J. Oh, I. Mishra, R. C. Devlin, and F. Capasso, "Polarization-insensitive metalenses at visible wavelengths," Nano Lett. **16**, 7229–7234 (2016).
61. H. Liang, Q. Lin, X. Xie, Q. Sun, Y. Wang, L. Zhou, L. Liu, X. Yu, J. Zhou, T. F. Krauss, and J. Li, "Ultrahigh numerical aperture metalens at visible wavelengths," Nano Lett. **18**, 4460–4466 (2018).